minerals

Article

Modelling of Acid Mine Drainage in Open Pit Lakes Using Sentinel-2 Time-Series: A Case Study from Lusatia, Germany

Delira Hanelli *, Andreas Barth, Gerald Volkmer and Martin Köhler

Beak Consultants GmbH, Am St. Niclas Schacht 13, 09599 Freiberg, Germany
* Correspondence: delira.hanelli@beak.de

Abstract: Strong acid mine drainage (AMD) processes in the flooded, formerly open pits in the Lusatia area present an enormous environmental challenge for the rehabilitation of the post-mining landscape. Extensive and costly monitoring is required for optimal AMD management and remediation planning and control. Because of the large size of the area and the dimension of the problem, the regular sampling can only provide limited point data, which needs to be extrapolated to the entire area. Consequently, the search for effective approaches for extrapolating the point data to the area of all water bodies is essential for rehabilitation success monitoring and for understanding the dependencies between AMD and environmental factors such as land use, weather conditions, geology, and hydrogeology. The main aim of this study was to investigate the suitability of Sentinel-2 multispectral imagery and artificial neural networks (ANNs) for the quantitative mapping of acid mine drainage (AMD) constituents, such as dissolved iron, pH value, and sulfate in large water bodies, for an area of approximately 7220 km^2 (the area of the pit lakes is about 185 km^2). Correlations between different chemical water parameters were also investigated. An extensive water monitoring dataset was used to train artificial neural networks for the identification of dependencies between the multispectral remote sensing data and the water quality ground measurements. Respective relationships have been identified, especially for dissolved iron and pH. These trained ANNs have been used to produce water quality maps with high spatial (10 $\times$ 10 m) and temporal (any cloud-free period) resolution, which show the wide variability of water quality in the different parts of the mining region. Concrete sources of AMD can be identified using the water quality maps of single lakes, and the success of sanitation measures such as liming was visualized. The approach opens many doors for the optimization of both the monitoring program and sanitation technology.

Keywords: acid mine drainage; Lusatia; artificial neural networks; remote sensing; multispectral imagery

Citation: Hanelli, D.; Barth, A.; Volkmer, G.; Köhler, M. Modelling of Acid Mine Drainage in Open Pit Lakes Using Sentinel-2 Time-Series: A Case Study from Lusatia, Germany. *Minerals* **2023**, *13*, 271. https://doi.org/10.3390/min13020271

Academic Editor: Teresa Valente

Received: 14 December 2022
Revised: 30 January 2023
Accepted: 8 February 2023
Published: 14 February 2023

1. Introduction

In the Lusatia area, lignite has been mined in large open cast pits for decades. In 2018, the annual lignite production was about 60 million metric tons [1], and it is mainly used for the production of electric energy (8000 MW of installed power). The mining and postmining landscapes cover approx. 7000 km^2, including numerous flooded former pits, remaining lakes, as well as active and inactive pits and channels used to release pumped out water to surface water bodies [2,3].

The two satellite images from 1985 and 2020 clearly show the dimensions of the lignite mining in Lusatia: in 1985, most of the pits are still dewatered, whereas the 2020 image shows the post-mining landscape with water-filled former pits and a few still active mines (Figure 1). The sulfidic sulfur contained in the lignite and in the host rocks (0.8–2.8%) [4] together with the dewatering caused groundwater movement, and the resulting big aerated zone led to strong acid mine drainage processes [5–8]. As a result, the water quality is poor and is marked by low pH values (up to 2) as well as high Fe^{3+} and $SO_4{}^{2-}$ concentrations.

Most of the pit lakes do not meet the water quality standards as prescribed for example by the EU Water Framework Directive for artificial and heavily modified water bodies [9].

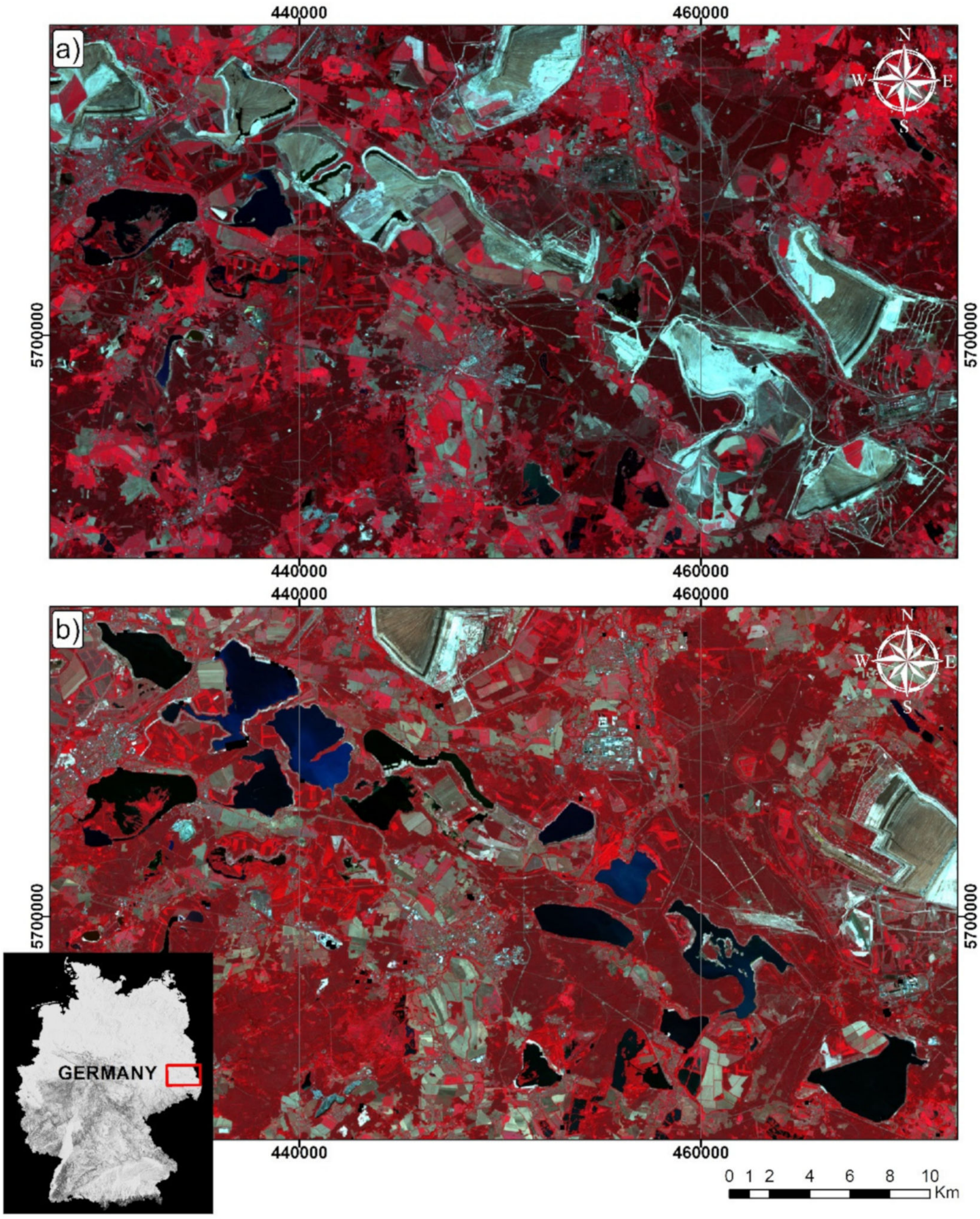

Figure 1. False-color images over the Lusatia region: (**a**) on the top, acquired in June 1985 by the Thematic Mapper (TM) on Landsat 5 (bands 4-3-2); (**b**) on the bottom, acquired in August 2020 by the Operational Land Imager (OLI) on Landsat 8 (bands 5-4-3). The false-color images were created using the Google Earth Engine platform.

Presently, the rehabilitation of the post-mining landscape is carried out by the Lausitzer und Mitteldeutsche Bergbau-Verwaltungsgesellschaft (LMBV). The LMBV undertakes big efforts to stabilize slopes and improve the water quality of the acid lake waters by continuously monitoring the groundwater and surface water quality at discrete sampling locations and by executing mitigation measures to neutralize acid mine drainage.

The identification and quantification of AMD in open pit lakes is of crucial importance for enacting prevention and mitigation measures in due time. In this context, remote sensing techniques offer the big advantage of continuous monitoring of the water quality over all of the water bodies. Together with the classical water monitoring at discrete sampling points, they allow for a very dense (both in space and time) observation of the AMD processes and their spatial and timely development, as well as allow for the success of rehabilitation measures.

In the present study, we have investigated the suitability of Sentinel-2 multispectral imagery and artificial neural networks (ANN) for the quantitative mapping of acid mine drainage (AMD) constituents in large water bodies. The Lusatia region offers a very suitable area for this case study due to the large variety of pit lakes and complexity of rock composition, groundwater movement, land cover, weather conditions, waste pile stability, and other AMD process-influencing parameters.

2. Used Data

2.1. Water Sampling Data

In this study, an extensive water monitoring dataset provided by the LMBV has been used as calibration data to train artificial neural networks. Between 2015 and 2020, the LMBV has allocated and analyzed over 9784 water samples at 199 surface water monitoring points (see Figure 2), whereas low pH values (2–4), high iron concentrations (up to 905 mg/L), and high sulfate concentrations (up to 3690 mg/L) have been recorded [10].

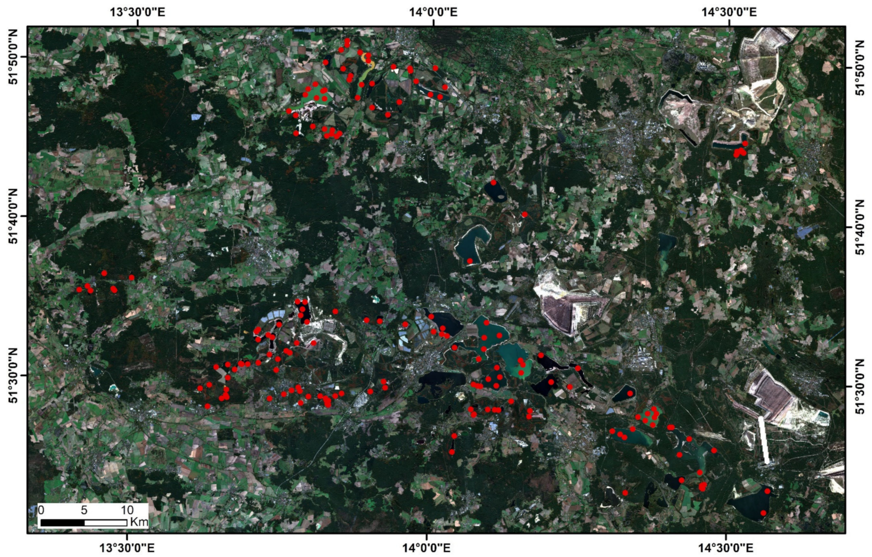

Figure 2. Location of the water monitoring points in the Lusatian post-mining water bodies.

Water samples were collected from the pit lakes during the circulation phase as well as during the stagnation phase from all three stratification zones: epilimnion, metalimnion, and hypolimnion.

The following water quality parameters, divided into three groups according to [11], have been analyzed:

1. Physical parameter: Electrical conductivity (µS/cm);
2. Chemical parameters: pH value, total Al (mg/L), Fe^{2+} (mg/L), Fe^{3+} (mg/L), total Fe (mg/L), total Mn (mg/L), $SO_4{}^{2-}$ (mg/L);
3. Biological parameter: Chl-a (µg/L).

In situ spectral reflectance measurements were not carried out.

2.2. Remote Sensing Data: Sentinel-2 Satellite Multispectral Imagery

Remote sensing is a powerful and cost-effective technique to collect frequent ground information for large areas in a short time. In this study, we elaborate the suitability of time-series Sentinel-2 multispectral imagery for the quantitative assessment of AMD in open pit lakes. The large-scale pit lakes encourage the use of free-of-charge, medium resolution multispectral imagery. Visible to shortwave infrared remote sensing has been widely used to monitor AMD mineralogy at mine sites. However, only a few studies have examined the spectral signatures of open pit water bodies from a remote platform [12–14].

The advantages of Sentinel-2 imagery compared with other free-of-charge optical remote sensing multispectral satellite data are summarized in the following:

1. Low-to-medium spatial resolution (4 × 10 m bands, 6 × 20 m bands, 3 × 60 m bands);
2. High temporal resolution (about 5 days on the Equator and 2–3 days over the Lusatia area) starting from 2015;
3. Channels in the visible (400–700 nm), near-infrared (NIR, 700–1100 nm), and short infrared (SWIR, 1100–2500 nm) parts of the electromagnetic spectrum (Figure 3).

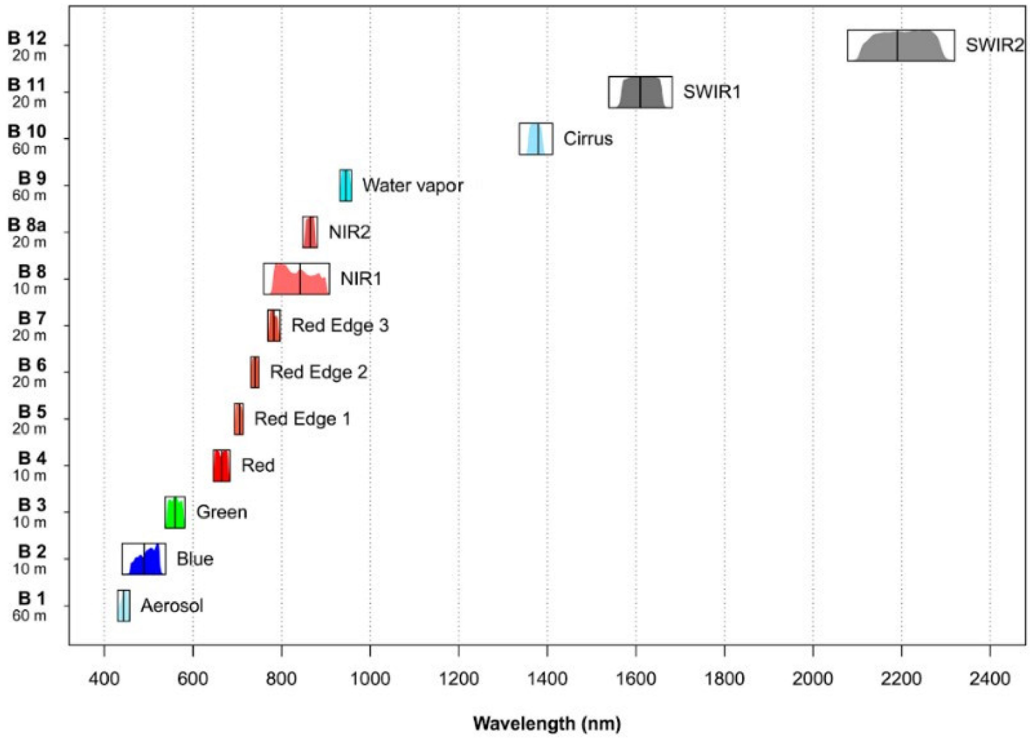

Figure 3. Characteristics of the multispectral instrument (MSI) on board Sentinel-2. Source: [15].

3. Methods

3.1. Water Sampling Data Processing

In this study, the focus is on samples collected in the epilimnion (depth of 0–15 m), which is the uppermost layer in a stratified lake (Figure 4).

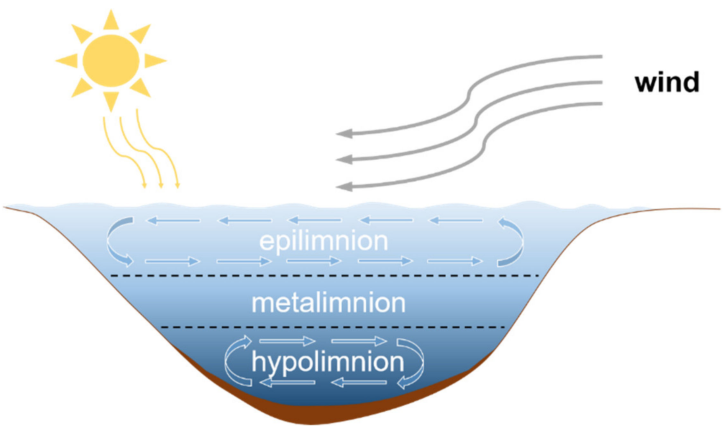

Figure 4. Lake stratification zones.

Samples collected closer than 10 m to the lake banks were excluded in order to avoid any influence of various optically active constituents (soil, vegetation, etc.) in the surface reflectance signal. Additionally, samples collected before 4 July 2015 were excluded due to the lack of Sentinel-2 satellite imagery. The water sampling data were used as calibration data to train and validate the supervised machine learning algorithms. In this study, we focus on three typical indicators of AMD:

1. Optically active constituent: iron concentrations (Fe^{3+});
2. Optically non-active constituents: pH, sulfate content ($SO_4{}^{2-}$)

The statistics of the water quality measurements for these indicators in the study area revealed dissolved iron concentrations (Fe^{3+}) from 0 to 905 mg/L, pH values ranging from 2 to 11, and sulfate concentrations ranging from 0 to 3690 mg/L.

The optically non-active parameters pH value and $SO_4{}^{2-}$ cannot be directly detected from the optical remote sensing data. Instead, this study investigated whether and how they can be modelled through patterns of optically active constituents.

Water bodies with high dissolved iron concentrations are marked by low pH values (<=4) (Figure 5). This dependency disappears if the Fe^{3+} concentrations are less than 0.3 mg/L.

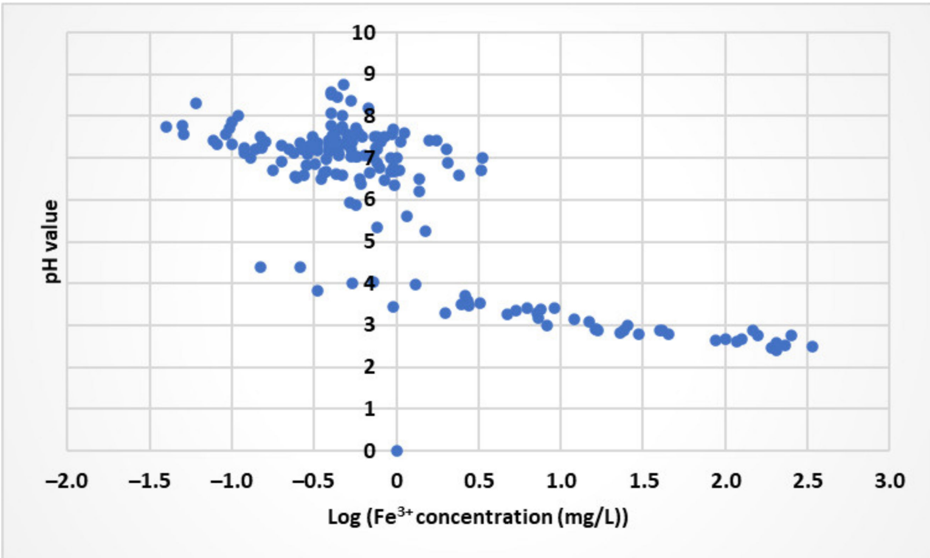

Figure 5. Plot of dependencies between Log (Fe^{3+}) and pH.

Figure 6 illustrates this dependency with an example of the measured Fe^{3+} and pH values for a selected area surrounding the Seewald See.

From 2015 until 2020, considerable changes in the water quality were observed at several places. For instance, at "Grüner See" (Figure 7) in July 2018, the pit water was characterized by low pH values (2.68) and high concentrations of sulfate and dissolved iron. In spring 2020, the pH value increased to 3.58 and the concentration of dissolved iron drastically sunk to 2.71 mg/L. The reason for this change is the water treatment with hydrated lime via a stationary system [16]:

$$CaCO_3\ (s) + H_2SO_4\ (aq) \rightarrow CaSO_4\ (s) + H_2O\ (l) + CO_2\ (g). \quad (1)$$

The sulfate content remained high because of the equilibrium with gypsum.

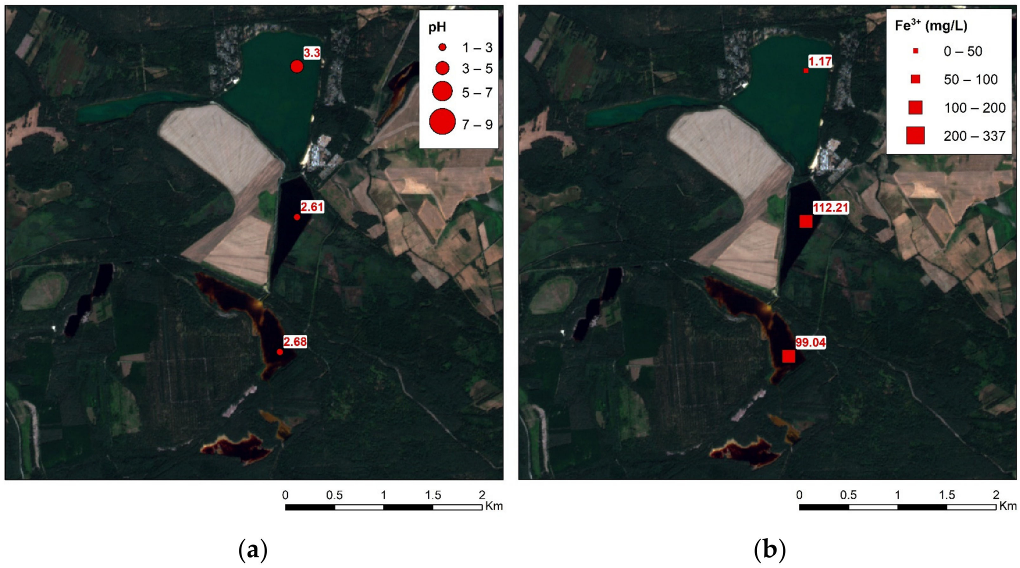

Figure 6. Measurements of (**a**) pH values and (**b**) Fe^{3+} concentrations for the selected samples of the study area, collected in September 2019. Background image is a Sentinel-2 RGB-composite of the visible bands acquired during 5–15 September 2019.

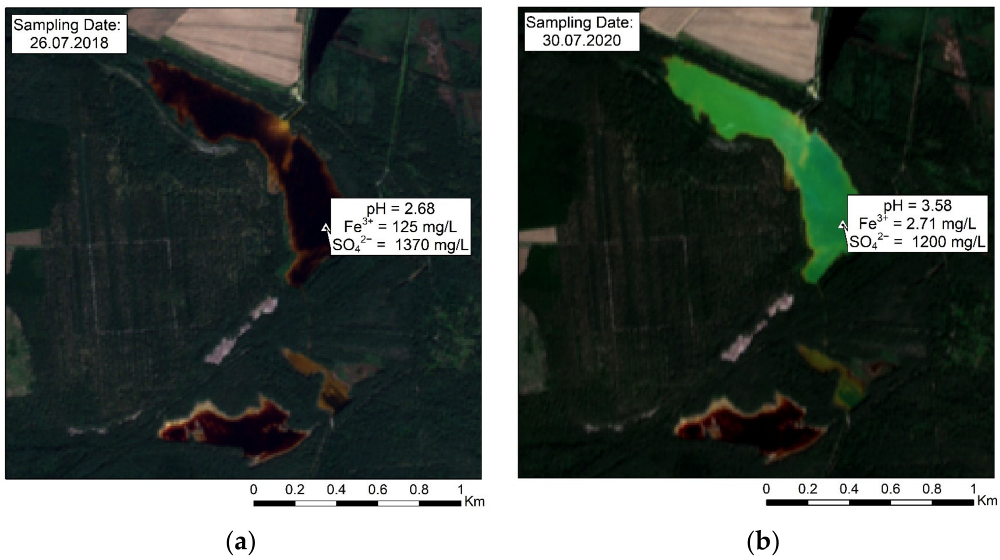

Figure 7. Measurements of pH value, Fe^{3+}, and $SO_4{}^{2-}$ in the "Grüner See", collected (**a**) in July 2018 with AMD and (**b**) in July 2020 after treatment of acid mine water with hydrated lime. Background images are natural color Sentinel-2 RGB-composites acquired during (**a**) 20 July–10 October 2018 and (**b**) 25 July–5 August 2020.

3.2. Sentinel-2 Data Acquistion and Processing

The spatial resolution of this study is set to 10 m to benefit from the medium spatial resolution of Sentinel-2 imagery.

The Sentinel-2 products are available as:

- Level-1C Top-Of-Atmosphere (TOA) starting from 2015;
- Level-2A Bottom-Of-Atmosphere (BOA) surface reflectance products starting from early 2018.

The atmospherically corrected BOA products were derived from the associated L1C products by applying the Sen2Cor processor in the Sentinel-2 toolbox. It is important to highlight that the Sen2cor processor was not designed for water bodies [17]. For this study, there were no in situ measured reflectance data collected and it was therefore not possible to directly validate the performance of the Sen2cor processor. Some examples in the literature (such as [18–20]) suggest that the TOA imagery for inland water quality analyses provided better results than the BOA atmospherically corrected imagery. In this study, both Sentinel-2 Level-1C TOA products and Level-2A BOA products were used, and their suitability for water quality analyses was compared.

Sentinel-2 products acquired during similar time intervals as the sampling data were first identified in the Copernicus Open Access Hub and then downloaded from the Earth Engine Data Catalog. The acquisitions of the Sentinel-2 satellites were selected by applying a temporal filter of ±5–10 days to the sampling date in order to ensure that the measured water quality parameters correspond to the recorded surface reflectance information of the selected satellite images. Optical analyses require the use of 100% cloud- and shadow-free satellite images; however, cloud- and shadow-free singular scenes are barely available in the study area. To overcome this issue, single satellite scenes were stacked in periods of 10–20 days using the widely temporal aggregation method of median values derived from time-series images [21]. Cloud and shadow areas are masked before the stacking process. This technology is implemented in Google Earth Engine's cloud-based computing platform [22], and the available scripts were customized for the purposes of this research.

Overall, 29 Sentinel-2 cloud- and shadow-free color-balanced mosaics were designed corresponding to the date of sampling. The individual images were rearranged in a single mosaic (Figure 8).

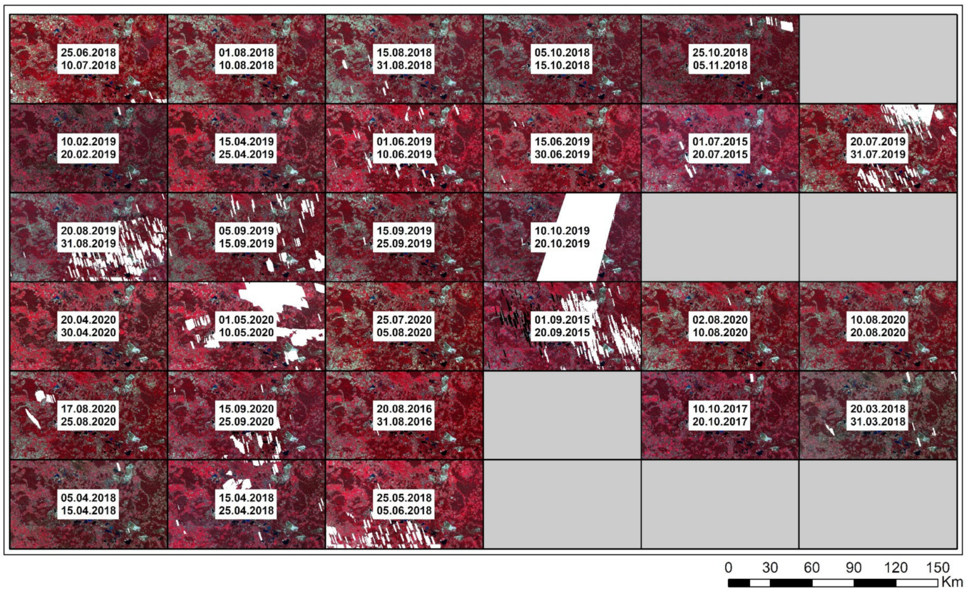

Figure 8. Single mosaic composed of 29 Sentinel-2 cloud- and shadow-free mosaics false-color images over the Lusatia region (bands 8-4-3).

The corresponding samples for each Sentinel-2 acquisition were also rearranged in a mosaic with the same principle. Table 1 provides the statistics of the sampling data.

Table 1. Statistics of the water quality measurements.

Parameter	No. of Samples	Min	Max	Mean	Median	Std
Fe^{3+} (mg/L)	210	0.05	337	13.69	0.83	46.89
$SO_4{}^{2-}$ (mg/L)	155	58.3	3120	1278.46	1290.00	709.67
pH	210	2.40	8.76	6.24	6.84	1.67

The water area was extracted using the modified normalized difference water index (mNDWI) proposed by [23]. The mNDWI discriminates the water surface from other land use classes and allows for a very efficient automatic extraction of water bodies (Figure 9). In this study, a threshold of 0.4 was empirically determined. The extracted water bodies and available samples were validated through an extensive quality control review of false-color Sentinel-2 imagery.

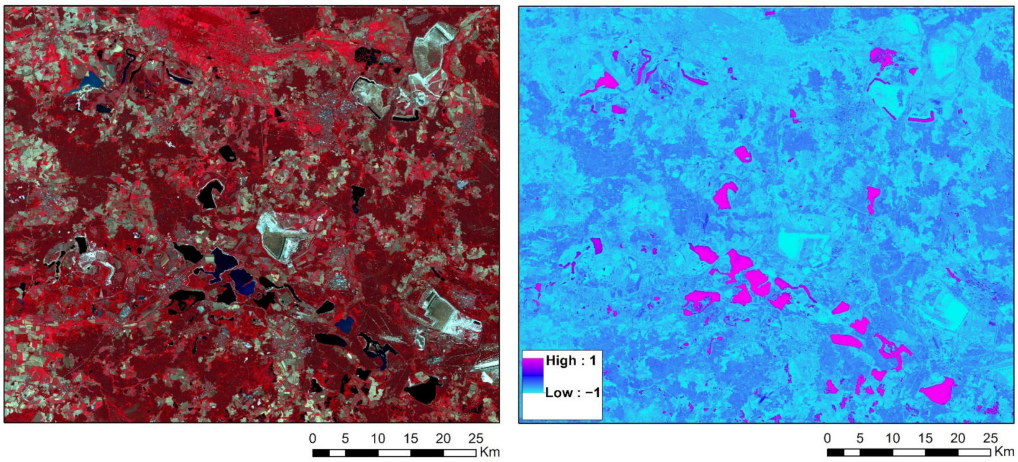

(**a**) (**b**)

Figure 9. (**a**) False-color image over the Lusatia region (bands 8-4-3) acquired in August 2020; (**b**) The mNDWI map.

Previous studies have presented many well-established algorithms to differentiate ferric iron-bearing minerals from remotely sensed imagery, such as, e.g.,

1. Ferric oxides (Fe^{3+}) index [24]

$$\mathrm{SWIR1/NIR2;} \tag{2}$$

2. Ferric iron (Fe^{3+}) index [25]

$$\mathrm{RED/GREEN;} \tag{3}$$

3. Gossan index [26]

$$\mathrm{SWIR1/RED;} \tag{4}$$

These algorithms were mainly established for applications on solid surfaces. In order to prove their suitability for water-related applications, they were estimated using the Sentinel-2 spectral reflectance bands for the mosaic image in Figure 8. The measured values of the Fe^{3+} concentrations and the calculated band ratios are graphically depicted in Figure 10. From their comparison, no correlation could be identified, indicating that the available band ratios for the differentiation of ferric iron-bearing minerals may not be suitable for water applications.

In this study, supervised machine learning artificial neural network algorithms were implemented to establish relationships between the surface reflectance and ferric iron-bearing minerals in water bodies.

The relation of the $SO_4{}^{2-}$ content in the gypsum and in the optically active components turbidity and total suspended solids (TSS) was also investigated. The turbidity of the surface waters was calculated using the well-established algorithm of the normalized difference turbidity index (NDTI), as follows:

$$\mathrm{NDTI} = (\mathrm{RED} - \mathrm{GREEN})/(\mathrm{RED} + \mathrm{GREEN}). \tag{5}$$

The algorithm for the qualitative estimation of the TSS in the surface waters was based on Sentinel-2 imagery (Level-2A BOA Product), proposed by [27]:

$$TSS = 2.272 + (RED/2.468) \times 2.154. \quad (6)$$

The performed analysis revealed the TSS to be slightly more suitable then NDTI at reflecting the changes in the sulfate concentration (Figures 11 and 12). However, the relationships between the surface reflectance and sulfate concentration in water bodies was further investigated using supervised machine learning algorithms of artificial neural networks.

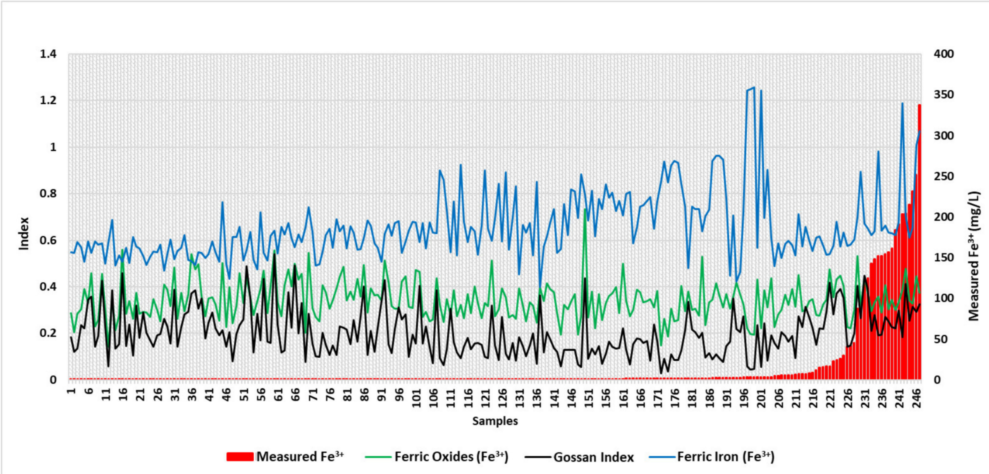

Figure 10. Comparison of Sentinel-2 indices and observed values of Fe^{3+} concentrations from water analysis. The samples are ordered according to their measured Fe^{3+} values.

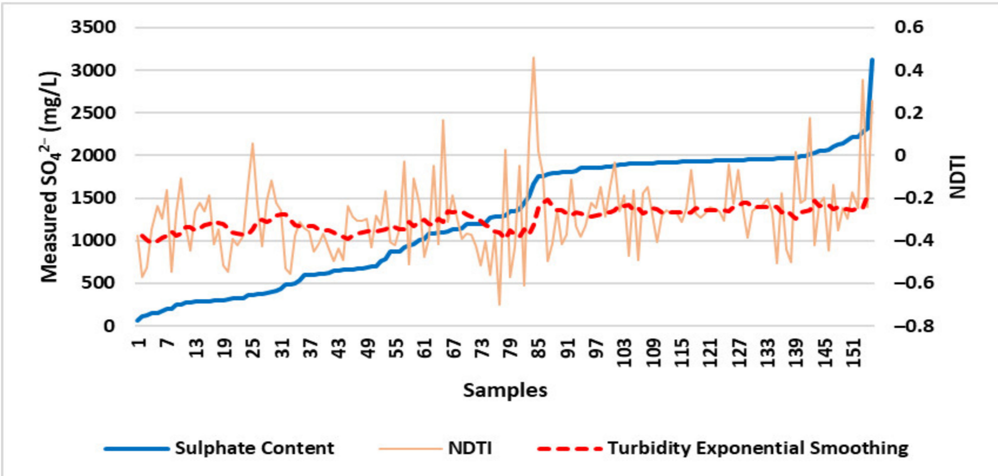

Figure 11. Comparison of the Sentinel-2 turbidity index (NDTI) and observed values of SO_4^{2-} content from water analysis.

3.3. Prediction Modelling Using Artificial Neural Networks

In this study, correlations between Sentinel-2 spectral reflectance bands and AMD constituents were investigated using the supervised machine learning algorithm of ANNs. Artificial neural networks of the multilayer perceptron type (MLP) were implemented in the advangeo® Prediction Software from Beak Consultants GmbH (www.advangeo.com (accessed on 10 November 2018)). The modelling and prediction software is developed to analyze complex relationships between a wide variety of spatial-influencing parameters and a given prognostic event or occurrence by using artificial intelligence methods within a geographic information system (GIS) environment [28]. The base principle is the ability of ANNs to generalize and learn from non-linear relationships and model natural complex processes and events, which are difficult or impossible to describe with analytical mathematics [29].

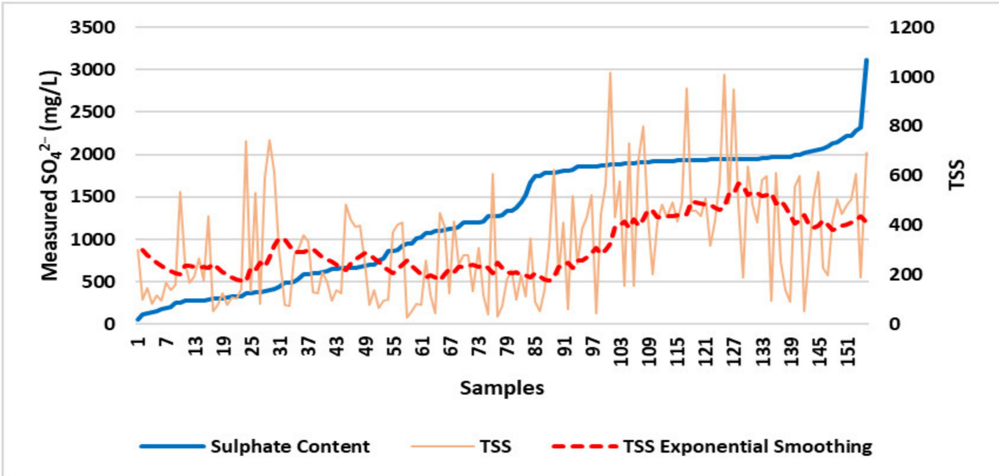

Figure 12. Comparison of Sentinel-2 total suspended solids (TSS) and observed values of SO_4^{2-} content from water analysis.

To model the distribution of iron concentration, pH value, and sulfate content across the Lusatian pit lakes, ANNs of the multilayer perceptron type were used according to the processing scheme in Figure 13.

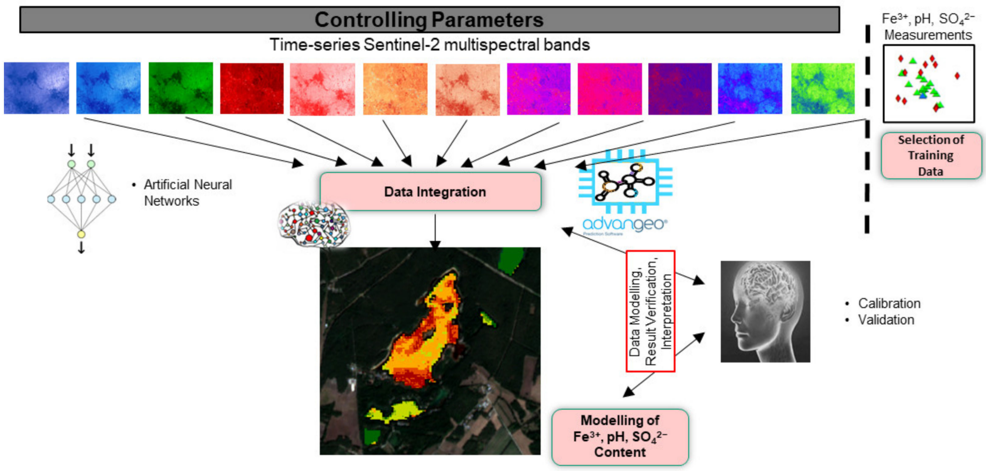

Figure 13. General processing schema of the prediction modelling using artificial neural networks.

The modeling process was limited to the identified water bodies, which were extracted as described in Section 2.2. The Sentinel-2 multispectral bands were used as controlling parameters. They were all resampled to 10 m using bilinear interpolation and were linearly scaled between 0 and 1.

Some important parameters of the used MLP are highlighted in the following:

- Network topology: input layer with a connection rate of 1 fully connected and 1 hidden layer with a predefined number of hidden neurons;
- Activation function: Sigmoid function with a steepness of 0.5;
- Learning algorithm: RPROP (derivative of the backpropagation algorithm);
- Weight initialization: 'Initialize' algorithm [30];
- Predefined stop parameters:
    - Maximum number of training epochs = 100;
    - Mean squared error (MSE) = 0.001.

4. Results

Several neural network models have been designed with the described principles and workflow. Here, the most significant models and results are presented.

4.1. Prediction Modelling of Dissolved Iron Concentration (Fe^{3+})

As revealed from the available sample data, the dissolved iron concentration values in the study area in the selected time intervals range from <0.01 to about 340 mg/L. For the first modelling approach, all available samples were taken into consideration as calibration data for the training scenario (Section 4.1.1). In the second approach (Section 4.1.2), representative samples for each lake (about 30% of the available data) were considered for the calibration of the machine learning algorithm. The rest of the sample data was used for validation.

4.1.1. Scenario 1: Use of All Available Samples as Calibration Data for the Training Scenario

Controlling parameters include Sentinel-2 multispectral bands of Level-1C and Level-2A products. The modelling was carried out using ANNs of the multilayer perceptron type. The validation and accuracy were assessed by analyzing the following parameters:

- Statistical evaluation: A comparison plot of the modelling results with the measured values of dissolved iron concentration, which suggested that the trained neural network has been able to reproduce the calibration data (Figure 14). The best results were obtained when using Sentinel-2 Level-2A BOA products as controlling parameters;
- The network MSE error: In both cases, the model error converges after approximately 10 iterations and the final error is below 0.2, indicating that the neural network is stable and accurate (Figure 15a).
- The model parameter weights: The model weights revealed the Sentinel-2 Level-2A B03 (Green), B02 (BLUE), and B11 (SWIR1) spectral bands to have the highest contribution for the modelling (Figure 15b).
- The distribution raster map: The prediction software delivers a distribution map in the value ranges of 0–1 (linearly scaled for 0–340), illustrating the distribution of dissolved iron concentration over the pit lakes in the study area. Analogously to the example in Figure 7, Figure 16 shows the distribution map for the Grüner See associated with AMD (July 2018) and after the neutralization of the acid mine water (July 2020).

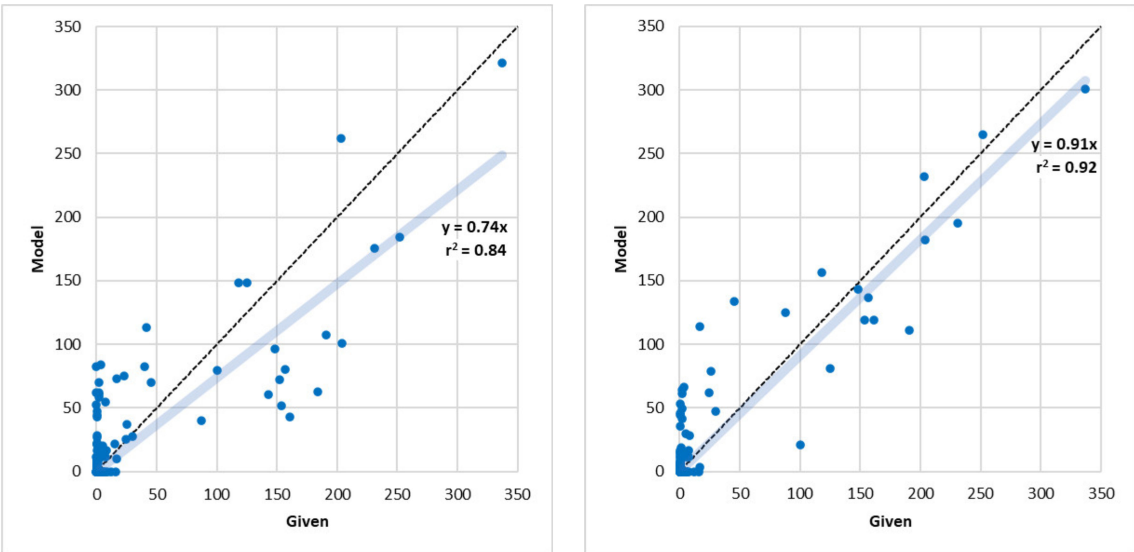

(**a**) (**b**)

Figure 14. Plot of given and modelled Fe^{3+} values based on (**a**) Sentinel-2 Level-1C TOA products and (**b**) Sentinel-2 Level-2A BOA products.

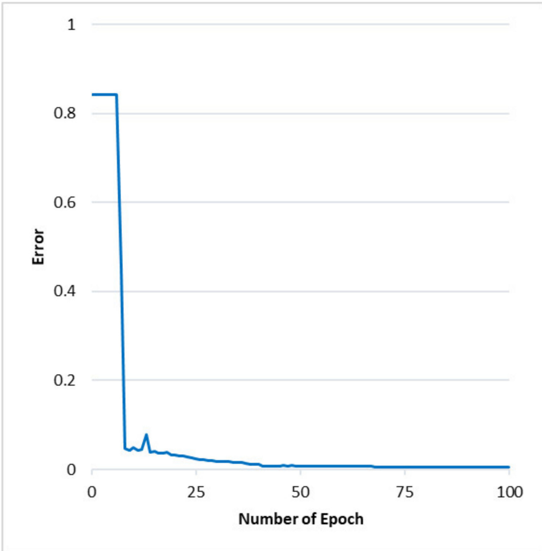

(**a**)

Input Layers	Garson
L2A\B12	0.55
L2A\B08	0.69
L2A\B06	0.7
L2A\B8A	0.72
L2A\B07	0.77
L2A\B09	1.03
L2A\B01	1.17
L2A\B05	1.75
L2A\B04	1.89
L2A\B11	2.18
L2A\B02	2.77
L2A\B03	6.8

(**b**)

Figure 15. (**a**) Plot of MSE and (**b**) weight parameters for the MLP based on Sentinel-2 Level-2A BOA products.

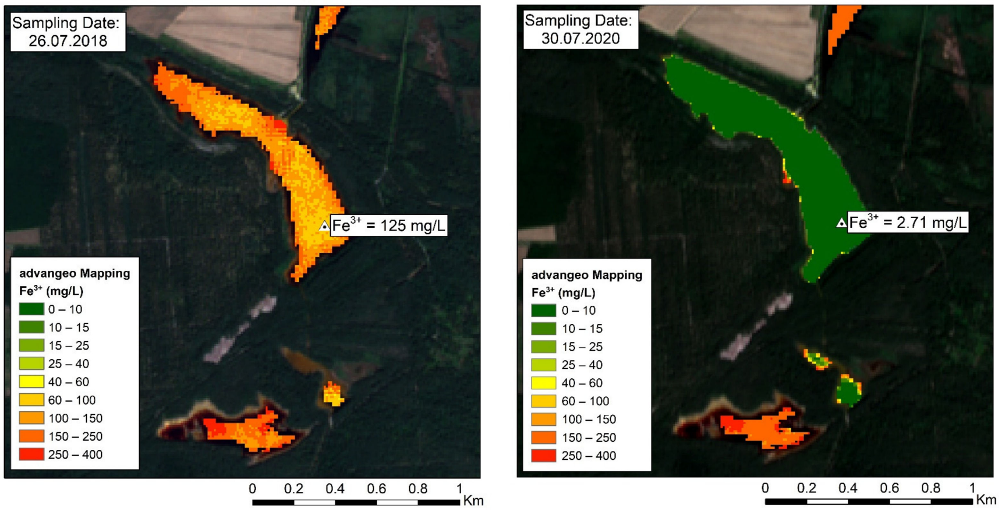

(**a**) (**b**)

Figure 16. Distribution map of Fe^{3+} in the "Grüner See" (**a**) in July 2018 with AMD and (**b**) in July 2020 after the neutralization of the acid mine water.

4.1.2. Scenario 2: Use of Representative Samples for Each Lake as Training Data

In this scenario, around 30% of the available sampling data has been used for the calibration. Their selection met two criteria: (i) each pit lake has to be represented by at least one measurement; (ii) if there are strong variations of dissolved iron concentration in one pit lake, extreme values have to be taken into consideration as calibration data.

Figure 17 shows the comparison plot of the given and modelled values for dissolved iron concentration for the training and validation samples using Sentinel-2 Level-2A TOA and BOA products. Overall, the trained neural network was able to reproduce the calibration and validation data. Moreover, in this scenario, the best results were achieved when using atmospherically corrected Sentinel-2 Level-2A BOA products.

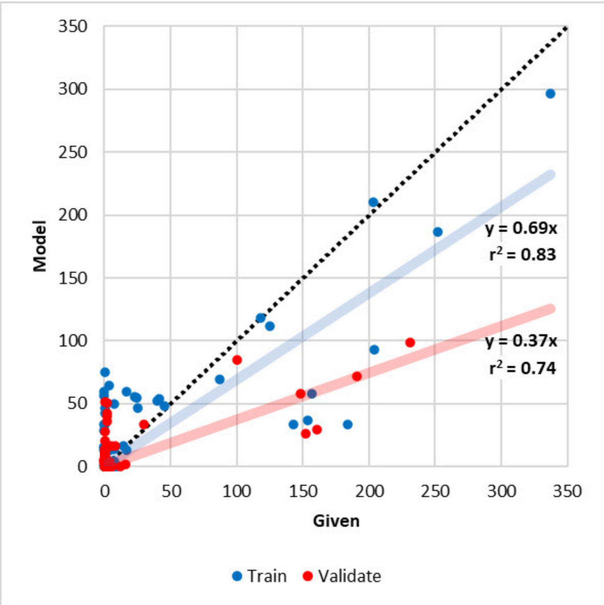

(**a**)

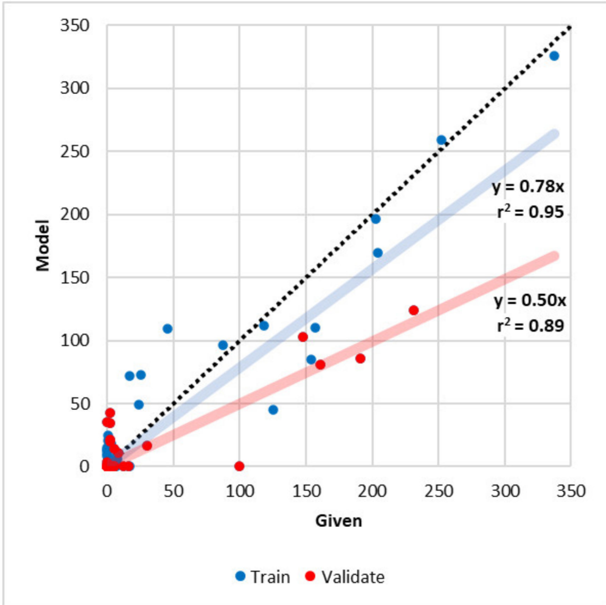

(**b**)

Figure 17. Plot of given and modelled Fe^{3+} values based on Sentinel-2 (**a**) Level-1C TOA and (**b**) Level-2A BOA products.

4.1.3. Comparison between Scenario 1 and Scenario 2

In order to prove the consistency between the two scenarios, the development of Fe^{3+} concentration over time have been tracked in some typical pit lakes associated with AMD (Figures 18–20). The linear graphs describe the Fe^{3+} concentration in the time-series from 20 March 2018–15 September 2020 in the Grüner See, Klärteich See, and Lugteich See, which was estimated based on the Level-2A BOA products with Scenario 1 and Scenario 2. Additionally, the recorded sampling measurements have been shown. The results from the two scenarios are mostly consistent, and one can distinguish clearly epochs of AMD (represented from high concentration of Fe^{3+}) and its neutralization. The concentration of Fe^{3+} has been clearly underestimated in the second scenario. This may be related to the reduced number of samples with high Fe^{3+} content used as calibration data in the second scenario.

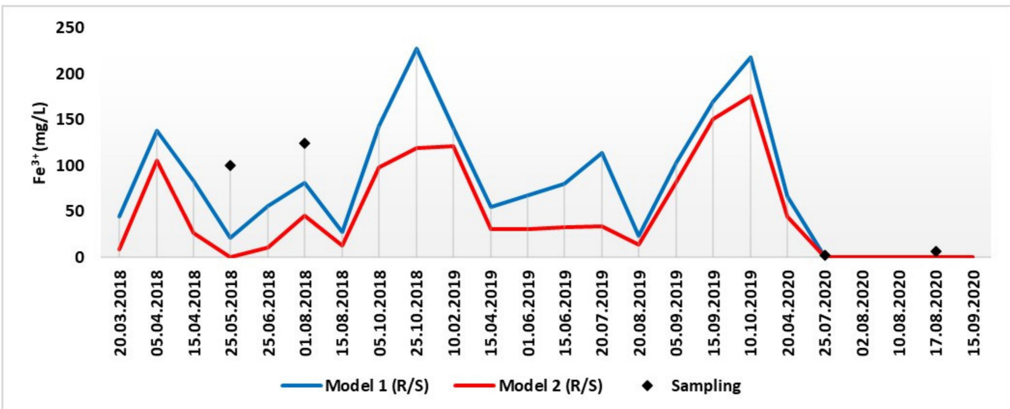

Figure 18. Development of Fe^{3+} concentration over time in the Grüner See.

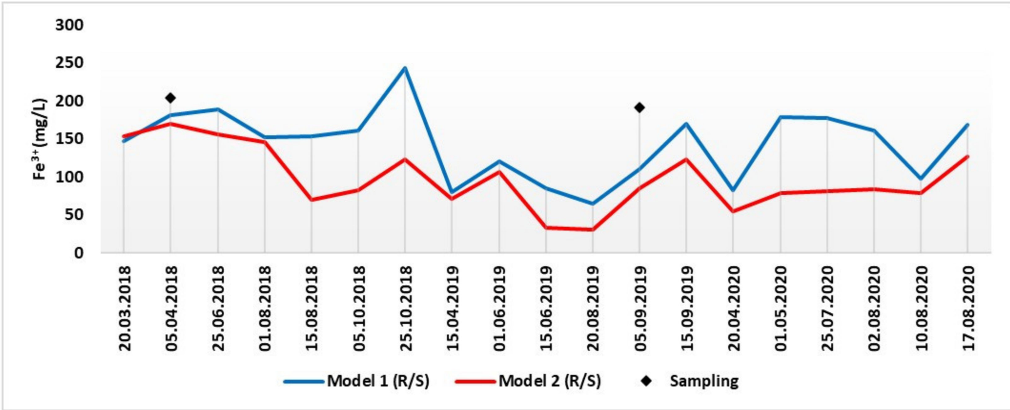

Figure 19. Development of Fe^{3+} concentration over time in the Klärteich See.

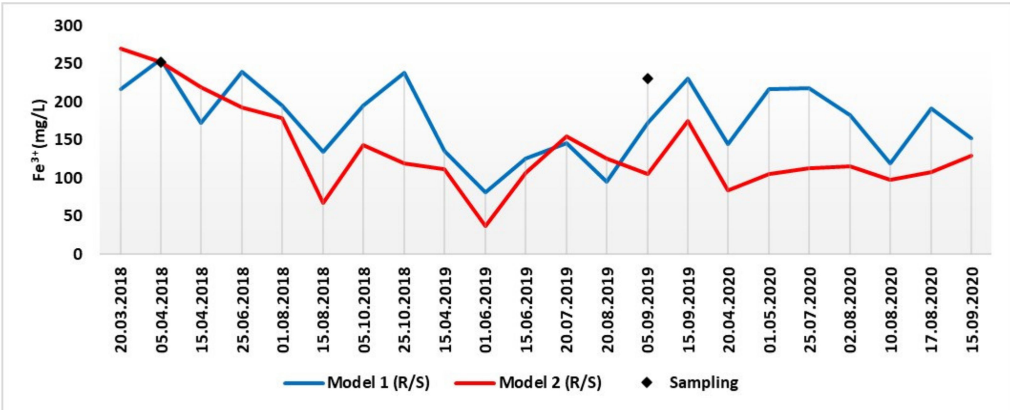

Figure 20. Development of Fe^{3+} concentration over time in the Lugteich See.

4.2. Prediction Modelling of pH

In contrast to Fe^{3+}, the pH value is an optically non-active constituent of AMD and therefore its modelling is more challenging. We tested the suitability of Sentinel-2 multispectral imagery to model pH values in water bodies. The correlation between Sentinel-2 bands and pH values has been shown to be especially strong for pH values in acidic to weakly-acidic water bodies (pH < 5) (Figure 21). In neutral to basic water bodies (pH $\geq$ 5), the modelled pH values show significant differences from the measured values. Consequently, no correlation could be found between the Sentinel-2 bands and the pH values.

To better understand these relationships, the pH values in acidic to weakly acidic water bodies (2–5) were used as calibration data in a new scenario. In this case, the ANNs were able to model the pH values with much better accuracy (Figure 22).

The obtained results based on Sentinel-2 Level-1C TOA and Level-2A BOA products look very similar, and it is hard to distinguish which one performed best. In both cases, the network error converges after approximately 50 iterations and the final error is below 0.2, indicating that the neural network is stable and accurate (Figure 23a). The model weights confirmed that the Sentinel-2 Level-2A B03 (Green), B02 (BLUE), and B11 (SWIR1) spectral bands have the highest contribution for the modelling. In comparison to the prediction models for Fe^{3+} concentration, in this case, band B01 was also given a significant weight.

Figure 24 shows the modelling distribution raster map of pH for the Grüner See. The map illustrates the differences of the pH values associated with AMD (July 2018) and after the neutralization of the acid mine water (July 2020).

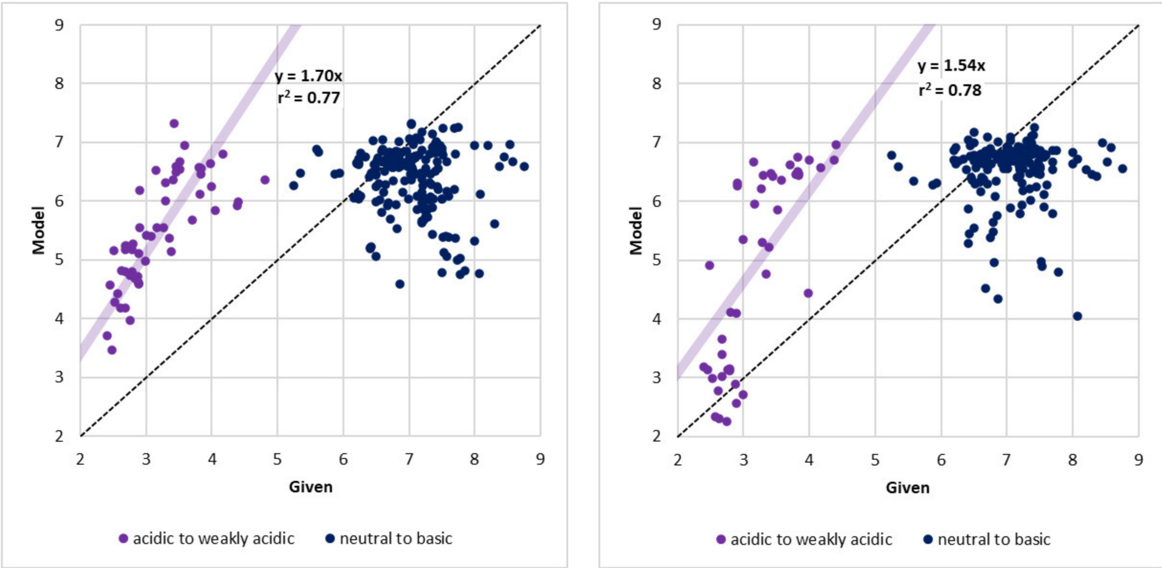

(**a**) (**b**)

Figure 21. Plot of given and modelled pH values based on Sentinel-2 (**a**) Level-1C TOA and (**b**) Level-2A BOA products.

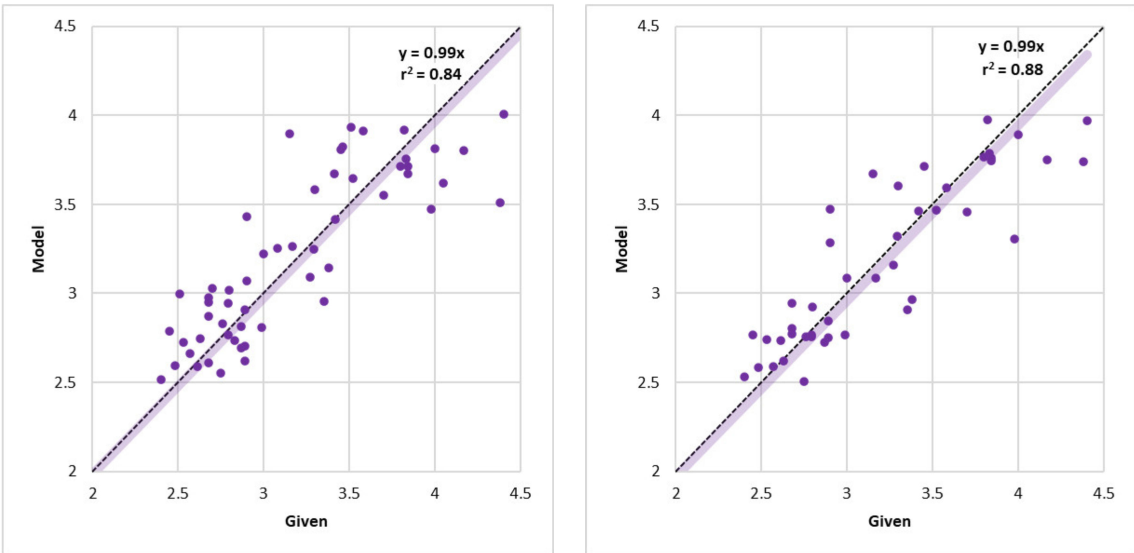

(**a**) (**b**)

Figure 22. Plot of given and modelled pH values in acidic to weakly acidic water bodies based on Sentinel-2 (**a**) Level-1C TOA and (**b**) Level-2A BOA products.

The correlation between Sentinel-2 bands and pH values in acidic to weakly acidic water bodies may be well-explained by the linear dependency between dissolved iron concentration and pH values, which was discussed in Section 2.1. As a result, the surface reflectance patterns of Fe^{3+} concentration influence the good result obtained in acidic to weakly acidic water.

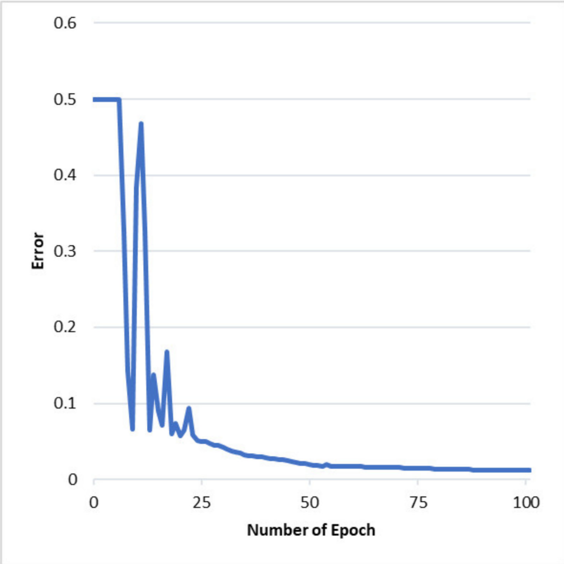

(**a**)

Input Layers	Garson
L2A\B12	0.75
L2A\B09	0.89
L2A\B8A	0.89
L2A\B07	1.10
L2A\B04	1.15
L2A\B08	1.24
L2A\B05	1.25
L2A\B06	1.27
L2A\B11	2.21
L2A\B03	2.31
L2A\B01	2.90
L2A\B02	5.04

(**b**)

Figure 23. (**a**) Plot of MSE and (**b**) weight parameters for the MLP based on Sentinel-2 Level-2A BOA products.

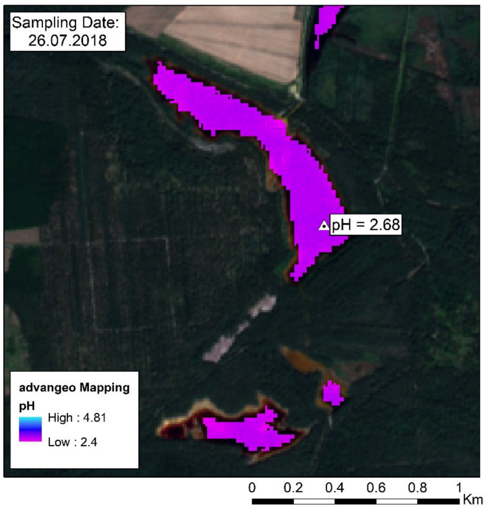

(**a**)

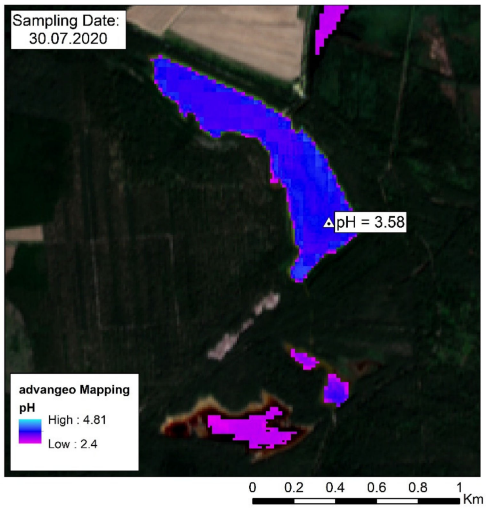

(**b**)

Figure 24. Distribution map of pH values in the "Grüner See" (**a**) in July 2018 with AMD and (**b**) in July 2020 after the neutralization of the acid mine water.

4.3. Prediction Modelling of Sulfate Concentration (SO_4^{2-})

Similar to the pH value, sulfate concentration is an optically non-active constituent of AMD. The suitability of Sentinel-2 multispectral imagery for modeling the sulfate concentration was tested on the water bodies. The results revealed that no correlation could be found between Sentinel-2 bands and sulfate concentration (Figure 25). Samples with sulfate concentrations higher than 1500 mg/L were used as calibration data in a separate ANN model; however, in this case, the results also did not show any correlation between Sentinel-2 bands and sulfate concentration. The reason is because the sulfate concentration is controlled either by the AMD processes or the equilibrium with gypsum.

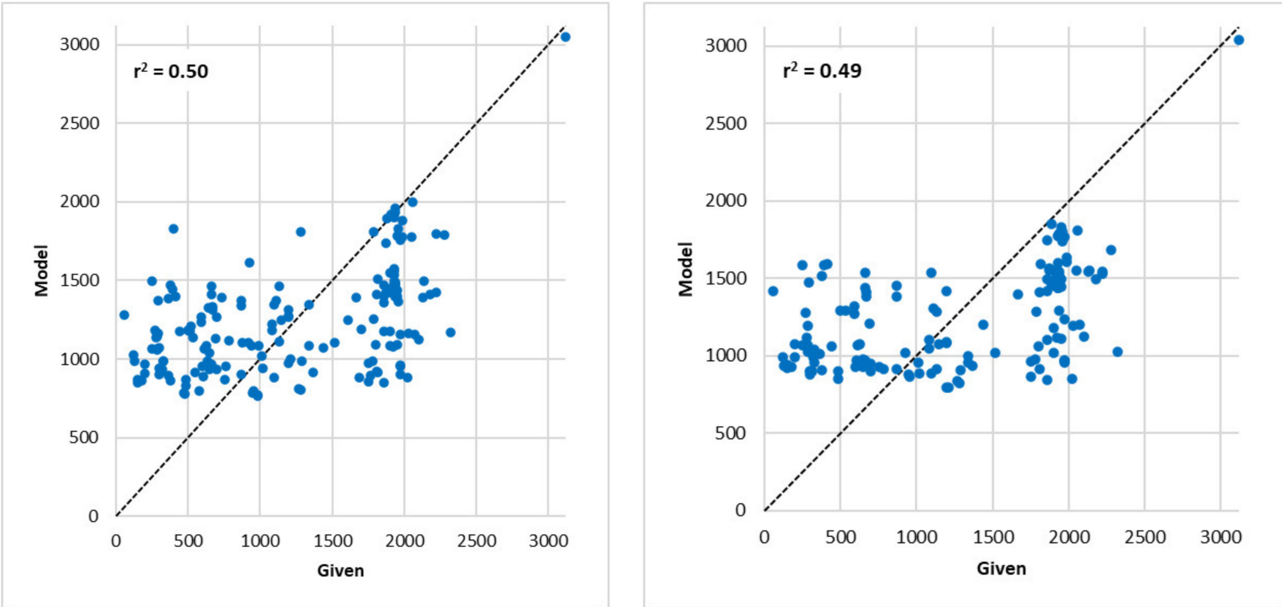

(**a**) (**b**)

Figure 25. Plot of given and modelled sulfate content values based on Sentinel-2 (**a**) Level-1C TOA and (**b**) Level-2A BOA products.

5. Discussion

Water environments are optically complex, and the signal that a remote sensing detector collects is a mixed signal composed of various optically active constituents from different sources [31]. For a water quality analysis based on remote sensing data, it is of crucial importance to use cloud- and cirrus-free images in pure water environments to avoid the influence of various optically active constituents (soil, vegetation, etc.) in the surface reflectance signal.

The proposed method provides an advanced approach to automatically identify and quantify iron concentration in water bodies using ANNs and low-to-medium resolution Sentinel-2 images. Careful selection of training samples and multispectral images proved to be key factors in establishing the ANN models. In this case study, many samples had to be left out of consideration due to their inconvenient location, e.g., proximity to the lake banks, samples in narrow small-scale lakes barely visible from the medium resolution imagery, etc.

The trained ANNs have been used to produce high spatial (10 $\times$ 10 m) and temporal resolution water quality maps showing the wide variability of water quality in different parts of the mining region. Considering the newly established dependencies, the approach opens many doors for the optimization of both the monitoring program and the sanitation technology.

On the other hand, the selection of cloud- and cirrus-free optical imagery has proved to be of critical importance for a proper calibration. In the Lusatia area, the selection of suitable imagery was especially challenging because of the presence of cirrus clouds, which compromised the quality of water pixels. However, reliable results could be obtained after an extensive quality control review of Sentinel-2 imagery.

An important aspect to consider is that the ANN results are limited to concentrations in a specific range defined from the calibration data, meaning that in this case, a quantitative analysis beyond this range cannot be extrapolated. In this context, discrete samples are still useful for properly calibrating the algorithms. However, the proposed method drastically reduces the need for continuous and discrete sampling and enables the mapping of the iron concentration throughout the entire area of the water bodies.

The suitability of other satellite remote sensing sensors such as WorldView-3 super-spectral, EnMAP hyperspectral data, or UAV-based high-resolution data can be further investigated in order to elaborate the influence of spatial, spectral, and temporal resolution in the modelling process.

Additionally, field spectro-radiometric measurements of surface reflectance could be useful information for validating the Sentinel data and obtained results, as these measurements are completely unaffected by the atmospheric conditions [32].

6. Conclusions

In this study, the established ANN model was used to perform several water quality analyses based on a time-series of Sentinel-2 data for all post-mining lakes in the Lusatia region. In this large and dynamically changing region, this workflow proved to be a fast and efficient method for an area-wide monitoring of the water quality in the post-mining lakes.

The area-wide AMD modelling allows for a better identification of the source and location of the contamination, therefore supporting the responsible authorities to take mitigation measures in due time. Figure 26 shows an example of AMD modelling in August 2020 in the Schlabendorfer See. The AMD map illustrates the distribution of the Fe^{3+} concentration based on remote sensing (R/S) data and provides information about the contamination source and its dilution within the water body. As indicated in Figure 26, the modelled AMD distribution map is consistent with the sample measurements.

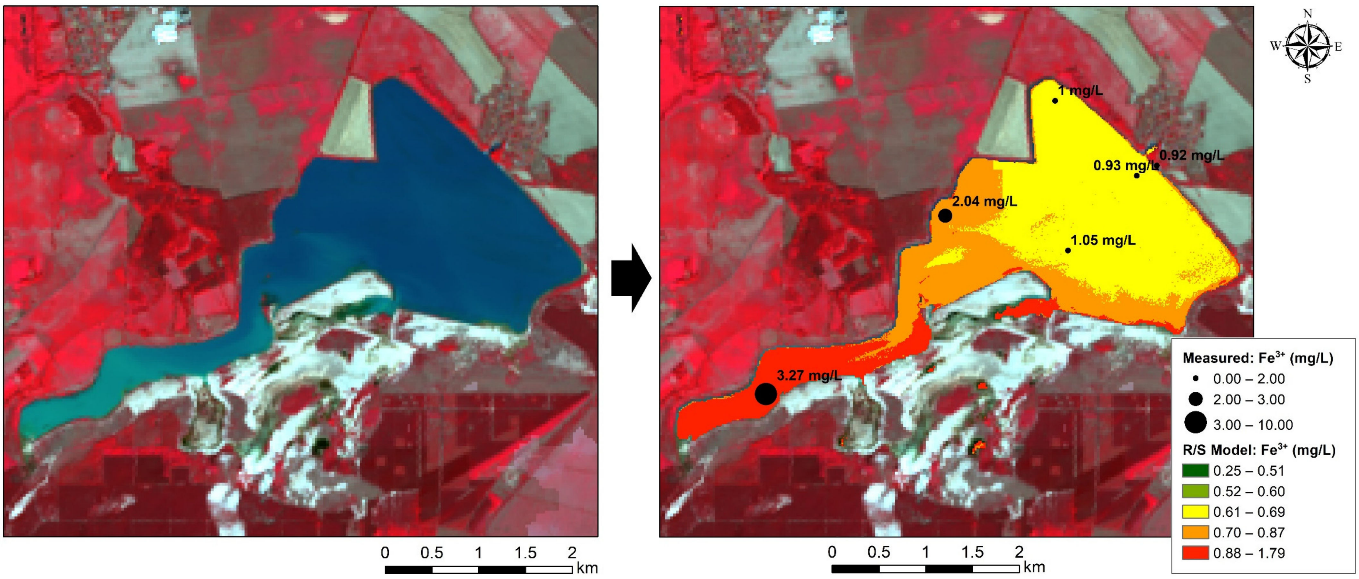

(**a**) (**b**)

Figure 26. (**a**) False-color image over the Schlabendorfer See (bands 8-4-3) acquired in August 2020. (**b**) The AMD distribution according to the R/S model.

The proposed approach not only provided reliable results for the concentration of (Fe^{3+}) but also for pH values in acidic to weakly acidic waters associated with AMD. These two parameters are strong indicators for the mapping of AMD in water bodies. Furthermore, the ANN model was trained and validated based on an extensive in situ database and was applied in a time-series over a wide variety of water bodies. Therefore, we conclude that this approach can be used cost-effectively and extensively for larger areas that are suspected to be the subject of AMD.

Author Contributions: Conceptualization, D.H., A.B. and G.V.; methodology, D.H., A.B. and G.V.; formal analysis, D.H. and A.B.; investigation, D.H. and A.B.; resources, D.H. and A.B.; data curation, D.H., A.B. and G.V.; writing—original draft preparation, D.H., G.V., M.K. and A.B.; writing—review and editing, D.H., A.B., G.V. and M.K.; visualization, D.H. and G.V.; supervision, G.V. and D.H.; project administration, G.V., D.H. and A.B.; funding acquisition, G.V., D.H. and A.B. All authors have read and agreed to the published version of the manuscript.

Funding: This research was co-funded by the Zentrales Innovationsprogramm des Mittelstandes (ZIM) of the German Federal Ministry of Economy and Energy, grant number 16KN057537.

Data Availability Statement: The data are not publicly available since they were generated under license for the current study. However, the data presented in this study are available on request from the corresponding author. Restrictions apply to the availability of water monitoring data. Data was obtained from the Lausitzer und Mitteldeutsche Bergbau-Verwaltungsgesellschaft and are available from the authors only with the permission of the Lausitzer und Mitteldeutsche Bergbau-Verwaltungsgesellschaft.

Acknowledgments: The authors are grateful to LMBV for providing the water monitoring data, which made this research study possible.

Conflicts of Interest: The authors declare no conflict of interest. The funders had no role in the design of the study; in the collection, analyses, or interpretation of data; in the writing of the manuscript, or in the decision to publish the results.

References

1. Statistik der Kohlenwirtschaft, e.V. Der Kohlenbergbau in der Energiewirtschaft der Bundesrepublik Deutschland im Jahre, 2018. Statistik der Kohlenwirtschaft, e.V.: Essen/Bergheim, Germany, 2019.
2. Schultze, M. The Filling and Remediation of Pit Lakes in Former Open Cast Lignite Mines. TU Braunschweig: Braunschweig, Germany, 2012.
3. Nixdorf, B.; Hemm, M.; Schlundt, A.; Kapfer, M.; Krumbeck, H. *Braunkohlentagebauseen in Deutschland: Gegenwärtiger Kenntnisstand über Wasserwirtschaftliche Belange von Braunkohlentagebaurestlöchern*; UBA-Texte, 35–01; Umweltbundesamt: Dessau-Roßlau, Germany, 2001.
4. Kahl, D. *Braunkohleverstromung im Lausitzer Revier*; Förderverein Kulturlandschaft Niederlausitz: Cottbus, Germany, 2009; ISBN 978-3-9811412-2-1.
5. Lazar, M.; Apostu, I.; Faur, F.; Rotunjanu, I. Factors influencing the flooding process of former coal open-pits. *Min. Miner. Depos.* **2021**, *15*, 124–133. [CrossRef]
6. Bazaluk, O.; Sadovenko, I.; Zahrytsenko, A.; Saik, P.; Lozynskyi, V.; Dychkovskyi, R. Forecasting Underground Water Dynamics within the Technogenic Environment of a Mine Field: Case Study. *Sustainability* **2021**, *13*, 7161. [CrossRef]
7. Rudakov, D.; Westermann, S. Analytical modeling of mine water rebound: Three case studies in closed hard-coal mines in Germany. *Min. Miner. Depos.* **2021**, *15*, 22–30. [CrossRef]
8. Schipek, M. Treatment of Acid Mine Lakes—Lab and Field Studies. Ph.D. Thesis, TU Bergakademie Freiberg, Freiberg, Germany, 2011.
9. Nixdorf, B.; Lessmann, D.; Deneke, R. Mining lakes in a disturbed landscape: Application of the EC Water Framework Directive and future management strategies. *Ecol. Eng.* **2005**, *24*, 67–73. [CrossRef]
10. LMBV. *Surface Water Monitoring Data*; Lausitzer und Mitteldeutsche Bergbauverwaltungsgesellschaft: Senftenberg, Germany, 2021.
11. Omer, N.H. Water Quality Parameters. IntechOpen. Available online: www.intechopen.com/chapters/69568 (accessed on 16 October 2019).
12. Davies, G.E.; Calvin, W.M. Quantifying Iron Concentration in Local and Synthetic Acid Mine Drainage: A New Technique Using Handheld Field Spectrometers. *Mine Water Environ.* **2016**, *2*, 299–309. [CrossRef]
13. Ismail, K.; Abdelkrim, A.; Abdelghani, B.; Mohammed, H.; Sabri El, M.; Kamal Ait, O.; Driss, E.; Abdelkhalek El Amrani, I.; Wafae, N. Evaluating the potential of Sentinel-2 satellite images for water quality characterization of artificial reservoirs: The Bin El Ouidane Reservoir case study (Morocco). *Meteorol. Hydrol. Water Manag.* **2018**, *7*, 31–39. [CrossRef]
14. Pizani, F.; Maillard, P.; Ferreira, A.; Amorim, C. Estimation of water quality in a reservoir from Sentinel-2 MSI and Landsat-8 OLI sensors. *ISPRS Ann. Photogramm. Remote Sens. Spat. Inf. Sci.* **2020**, *3*, 401–408. [CrossRef]
15. Immitzer, M.; Vuolo, F.; Atzberger, C. First Experience with Sentinel-2 Data for Crop and Tree Species Classifications in Central Europe. *Remote Sens.* **2016**, *8*, 166. [CrossRef]
16. LMBV. *Daten, Fakten und Informationen zur Bergbausanierung und Verwaltung in der Lausitz und Mitteldeutschland im Jahr 2020*; Sanierungsbericht 2020; Lausitzer und Mitteldeutsche Bergbauverwaltungsgesellschaft: Senftenberg, Germany, 2021.
17. Warren, M.; Simis, S.; Martinez-Vicente, V.; Poser, K.; Bresciani, M.; Alikas, K.; Spyrakos, E.; Giardino, C.; Ansper, A. Assessment of atmospheric correction algorithms for the Sentinel-2A Multispectral Imagery over coastal and inland waters. *Remote Sens. Environ.* **2019**, *225*, 267–289. [CrossRef]

18. Toming, K.; Kutser, T.; Laas, A.; Sepp, M.; Paavel, B.; Nõges, T. First Experiences in Mapping Lake Water Quality Parameters with Sentinel-2 MSI Imagery. *Remote Sens.* **2016**, *8*, 640. [CrossRef]
19. Kallio, K.; Attila, J.; Härmä, P.; Koponen, S.; Pulliainen, J.; Hyytiäinen, U.; Pyhälahti, T. Landsat ETM+ images in the estimation of seasonal lake water quality in boreal river basins. *Environ. Manag.* **2008**, *42*, 511–522. [CrossRef] [PubMed]
20. Kutser, T. The possibility of using the Landsat image archive for monitoring long time trends in coloured dissolved organic matter concentration in lake waters. *Remote Sens. Environ.* **2012**, *123*, 334–338. [CrossRef]
21. Phan, T.; Kuch, V.; Lehnert, L. Land Cover Classification using Google Earth Engine and Random Forest Classifier—The Role of Image Composition. *Remote Sens.* **2020**, *12*, 2411. [CrossRef]
22. Gorelick, N.; Hancher, M.; Dixon, M.; Ilyushchenko, S.; Thau, D.; Moore, R. Google Earth Engine: Planetary-scale geospatial analysis for everyone. *Remote Sens. Environ.* **2017**, *202*, 18–27. [CrossRef]
23. Du, Y.; Zhang, Y.; Ling, F.; Wang, Q.; Li, W.; Li, X. Water Bodies' Mapping from Sentinel-2 Imagery with Modified Normalized Difference Water Index at 10-m Spatial Resolution Produced by Sharpening the SWIR Band. *Remote Sens.* **2016**, *8*, 354. [CrossRef]
24. Segal, D. Theoretical Basis for Differentiation of Ferric-Iron Bearing Minerals, Using Landsat MSS Data. In Proceedings of the Symposium for Remote Sensing of Environment, 2nd Thematic Conference on Remote Sensing for Exploratory Geology, Fort Worth, TX, USA, 6–10 December 1982.
25. Rowan, L.C.; Mars, J.C. Lithological mapping in the Mountain Pass, California area, using Advanced Spaceborne Thermal Emission and Reflection Radiometer (ASTER) data. *Remote Sens. Environ.* **2003**, *84*, 350–366. [CrossRef]
26. Volesky, J.; Stern, B.; Johnson, P.R. Geological control of massive sulfide mineralization in the Neoproterozoic Wadi Bidah shear zone, southwestern Saudi Arabia, inferences from orbital remote sensing and field studies. *Precambrian Res.* **2003**, *123*, 235–247. [CrossRef]
27. De Lucia Lobo, F.; Leão de Moraes Novo, E.M.; Faria Barbosa, C.C.; de Vasconcelos, V.H.F. Monitoring Water Siltation Caused by Small-Scale Gold Mining in Amazonian Rivers Using Multi-Satellite Images. IntechOpen. Available online: www.intechopen.com/chapters/62698 (accessed on 5 November 2018).
28. Barth, A.; Knobloch, A.; Noack, S.; Schmidt, F. Neural Network-Based Spatial Modeling of Natural Phenomena and Events. In *Systems and Software Development, Modeling, and Analysis: New Perspectives and Methodologies*; Khosrow-Pour, M., Ed.; IGI-Global: Hershey, PA, USA, 2014; pp. 186–211. ISBN 13: 9781466660984.
29. Haykin, S. *Neural Networks: A Comprehensive Foundation*; Prentice Hall PTR: Upper Saddle River, NJ, USA, 1998; ISBN 978-0-13-273350-2.
30. Nguyen, D.W.B. Improving the learning speed of 2-layer neural networks by choosing initial values of the adaptive weights. In Proceedings of the 1990 IJCNN International Joint Conference on Neural Networks, San Diego, CA, USA, 17–21 June 1990; pp. 21–26.
31. Brando, V.E.; Dekker, A.G. Satellite Hyperspectral Remote Sensing for Estimating Estuarine and Coastal Water Quality. *IEEE Trans. Geosci. Remote Sens.* **2003**, *41*, 1378–1387. [CrossRef]
32. Padró, J.-C.; Muñoz, F.J.; Ávila, L.A.; Pesquer, L.; Pons, X. Radiometric correction of Landsat-8 and Sentinel-2A scenes using drone imagery in synergy with field spectroradiometry. *Remote Sens.* **2018**, *10*, 1687. [CrossRef]